ACS Catalysis

Research Article

Cite This: ACS Catal. 2018, 8, 9711−9721

pubs.acs.org/acscatalysis

TiH Hydride Formed on Amorphous Black Titania: Unprecedented Active Species for Photocatalytic Hydrogen Evolution

Sicong Ma,[†] Si-Da Huang,[†] Ya-Hui Fang,[‡] and Zhi-Pan Liu*[,†]

[†]Collaborative Innovation Center of Chemistry for Energy Material, Shanghai Key Laboratory of Molecular Catalysis and Innovative Materials, Key Laboratory of Computational Physical Science, Department of Chemistry, Fudan University, Shanghai 200433, China

[‡]School of Chemical and Environmental Engineering, Shanghai Institute of Technology, Shanghai 201418, China

Supporting Information

ABSTRACT: Amorphous structures are often good catalysts for their large varieties of exposed surface sites, but the characterization of the catalytic sites has long been a great challenge for both theory and experiment. One such interesting example is the recently synthesized "black TiO_2" via the hydrogenation of TiO_2 nanoparticles, which has an amorphous shell and crystalline core, and exhibits high hydrogen evolution reaction (HER) activity in the visible-light photocatalytic water splitting. Here, we utilize our recently developed theoretical tool, namely, the stochastic surface walking global optimization with neural network potential followed by first-principles validation, to quantitatively determine the thermodynamic phase diagram of TiO_2 in contact with H_2 at different temperatures and pressures. Among a number of anatase surfaces, we show that, only on a ridged anatase (112) surface, a local high H coverage, 0.69 ML, can be gradually built up accompanied by the surface amorphization. This high H coverage not only renders the black color of the amorphous TiO_2 but also provides an unprecedented low-energy reaction channel for the HER: a transient Ti−H hydride becomes likely to form on exposed Ti atoms, and its reaction with neighboring OH has much lower barrier, i.e., 0.6 eV, compared to the traditional H coupling channel via two surface OH groups (barrier >1.6 eV). Our results not only provide deep insights into the surface species and reactions that are unique to amorphous materials, but also demonstrate that the global sampling with neural network potential holds a great promise for solving complex structures under realistic reactions.

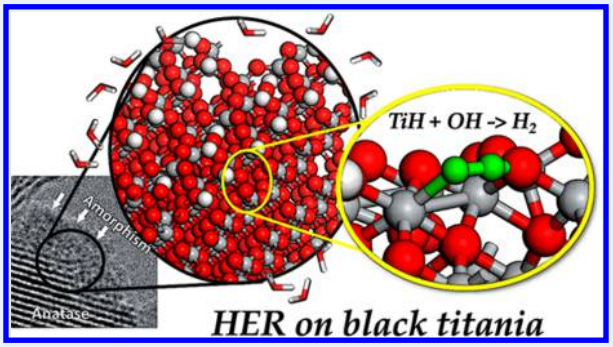

KEYWORDS: *TiH hydride, hydrogenation, black TiO_2, amorphization, neural network, DFT*

1. INTRODUCTION

Black titania (TiO_2) represents a promising visible-light photocatalyst, exhibiting strong absorption in the entire visible-light spectrum and high hydrogen evolution reaction (HER) activity.[1] It was found that the catalyst can be synthesized under versatile reaction conditions by treating pristine TiO_2 material with H-containing reductants (e.g., H_2 or $NaBH_4$),[2−4] and the reported photocatalytic activity for the HER is exceptional, being several orders magnitude greater than those of common semiconductor photocatalysts, e.g., commercial TiO_2 P25.[5] Despite extensive studies on this material, the surface structure and, more importantly, the active sites of black TiO_2 for the HER are, however, largely unknown. It is observed that the black titania involves complicated structure evolution during hydrogenation, associated with a series of phase transitions from TiO_2 to TiO_xH_y that lead to the surface amorphization. To probe the atomic nature for amorphous surfaces remains a highly challenging task in chemistry and material science, not even mentioning the identification of the catalytic active site for the HER.

For the preparation of black titania, the thermal hydrogenation method, as introduced by Chen et al.,[1] is perhaps the most popular approach, although the synthesis conditions can vary significantly from experiment to experiment, i.e., temperature from 15 to 700 °C, the H_2 pressure from 7 Mbar H_2 atmosphere to 5% H_2/N_2 mixture gas at ambient pressure, and the reaction time from 1 h to 15 days.[4,6] These as-synthesized materials exhibit commonly a core−shell structure with the amorphous shell, of a few nanometers thickness, coated on the anatase crystals (Figure 1),[1,3,6−9] but they exhibit quite different HER activity. For example, the HER activity of the black TiO_2 obtained under 35 bar hydrogen and room temperature (Figure 1) is up to 3.94 mmol h^{-1} g^{-1}, much larger than 0.19 mmol h^{-1} g^{-1} for commercial P25.[6] Similarly, the hydrogenated anatase TiO_2 nanotubes from high-temperature H_2 treatment (H_2, 20 bar, 500 °C, for 1 h) had a high open circuit photocatalytic HER rate (7 μmol h^{-1} cm^{-2}). By contrast, the samples produced from

Received: August 2, 2018
Revised: September 5, 2018
Published: September 11, 2018

DOI: 10.1021/acscatal.8b03077
ACS Catal. 2018, 8, 9711−9721

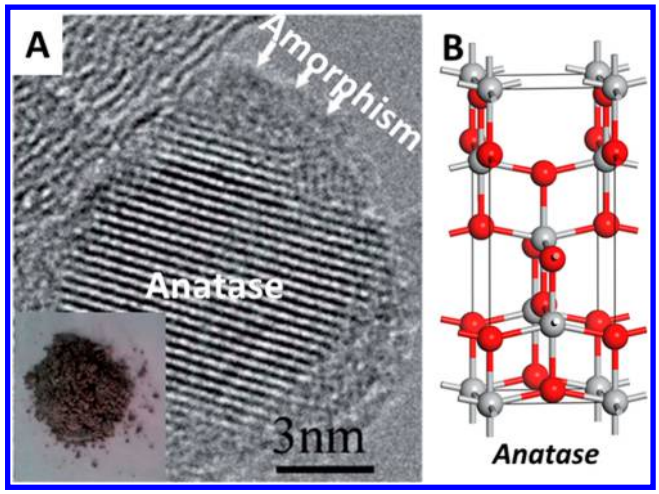

Figure 1. Black anatase TiO_2 structure synthesized from high-pressure hydrogenation. (A) High-resolution TEM image of the hydrogenated black P25 from ref 6, with permission (Copyright 2014, The Royal Society of Chemistry). (B) Crystal structures of anatase TiO_2 ($I4_1/AMD$, 141). Ti, gray balls; O, red balls.

atmospheric pressure H_2/Ar annealing show no HER activity.[10] Apparently, the (amorphous) shells that are structurally different under different synthetic conditions should play critical roles in catalyzing the HER.

Various experimental techniques have been attempted to characterize the structure of active black TiO_2 anatase materials. For the high-temperature (e.g., >400 °C) treatment, it was assumed that the amorphization will produce the TiO_x ($x < 2$) composite. Indeed, the oxygen vacancies (O_v) are confirmed by several groups using electron spin resonance in experiments.[3,10−12] Theoretically, by using reactive force-field molecular dynamics simulations, Selcuk et al. recently revealed that the O_v can be created on anatase TiO_2 nanoparticles upon the reaction of surface H with surface oxygen at high temperatures (800 K in simulation) which initiates the surface disordering.[13]

On the other hand, the nature for the low-temperature (<200 °C) amorphization is much more puzzling, both on the kinetics and on the amorphous structures. Since the reduction peak from H_2-temperature-programmed reduction of titania is generally above 400 °C,[14,15] the presence of O_v is largely ruled out for the black titania obtained with the low-temperature H_2 treatment. Instead, a TiO_2H_x model was proposed to account for the amorphous shell obtained at the low temperatures. Interestingly, the presence of the H atom has indeed been detected by X-ray photoelectron spectroscopy (XPS), Fourier transform infrared, and ^{1}H nuclear magnetic resonance. For example, the shoulder peaks in the O 1s and Ti 2p XPS spectra are observed in hydrogenated black TiO_2 nanoparticles, nanowires, etc., which are assigned to surface OH and TiH, respectively.[1,16] Although the TiO_2H_x structures are present from experiment, the energetic data from recent quantum mechanics calculations, however, do not support this picture because of highly positive formation energies of bulk TiO_2H_x.[17] This may well be due to the long-known "structure-gap" problem that theoretical analyses were performed on pristine TiO_2 bulks and surfaces, which are far from the amorphous layer observed in experiment. To resolve the HER active sites on the amorphous TiO_2 shell, not only an accurate potential energy surface (PES) but also a proper sampling for all surface structural configurations, ranging from crystals to amorphous, are essential. New tools are thus urgently called for to resolve the atomic structure of the amorphous shell that grows under reaction conditions.

Here, by using machine learning and global sampling followed by first-principles validation, we resolve the surface structure of anatase under H_2 pressure, from which the active site for hydrogen evolution is determined. Our approach is based on the recently developed SSW-NN as implemented in LASP code,[18] where the stochastic surface walking (SSW) global optimization combines with high-dimensional neural network (NN) potential to achieve fast PES global exploration. The low-energy structure candidates from SSW-NN exploration are then fully converged using plane-wave DFT calculations with high-accuracy setups. With a large pool of bulk and surface structures from first-principles, we are able to establish for the first time the thermodynamic phase diagrams of TiO_2 in contact with H_2, where bulk or surface TiO_xH_y with varied compositions is found to present under different reaction conditions. Importantly, we show that the amorphization is thermodynamically driven, and it leads to the ability of the anatase surface to accommodate a high coverage of hydrogen, which allows for the formation of the TiH hydride that is the key species for the catalytic HER.

2. METHODS AND CALCULATION DETAILS

2.1. SSW-NN Methods. To probe the nature of the amorphous shell after TiO_2 hydrogenation and identify the active site for the HER, the dynamics of the TiO_2 surfaces under reductive condition must be investigated, which calls for a reliable and efficient tool to sample the PES. Although density functional theory (DFT) calculations emerged as a reliable tool for PES construction, the poor scaling and the high computational demand severely restrict its application in large systems with complex PES (e.g., >100 atoms). In this work, we utilize the recently developed SSW-NN method to construct the NN global PES of TiO_xH_y and then utilize the NN PES to study their dynamics properties. The SSW method is an automated approach to explore the multidimensional PES, and its ability to identify the global minimum of complex covalent systems has been demonstrated recently.[19−23] The combination of SSW with NN potential allows the generation of highly transferable NN global PES. It should be emphasized that the NN simulation is at least 3−4 orders of magnitude faster than DFT, while keeping the accuracy in energy and force comparable with those from DFT. As reported in the previous work,[24] the SSW-NN method to explore PES can be divided into three steps: (a) global data set generation using SSW global optimization based on DFT calculations; (b) NN PES fitting; and (c) SSW global optimization using NN PES. These three steps are briefly summarized below (more details can be found in the Supporting Information, SI).

2.1.a. Global Data Set Generation. For the acquisition of the global data set for TiO_xH_y, 24 SSW simulations in total for TiO_xH_y, including bulks, layers, and clusters as the initial structures, were performed using plane-wave DFT calculations. The system size of these 24 simulations varies from 11 to 16 atoms per cell and has different Ti:O:H ratios, i.e.; Ti_4O_7; Ti_4O_8; and $Ti_4O_8H_x$, x = 1−4. Apart from these basic data, we also supplement the data set by performing SSW simulations for larger TiO_xH_y systems, i.e., $Ti_8O_{16}H_x$, x = 1−4, and molecular systems, i.e., H_2, H_2O. Overall, these SSW simulations generate more than 500 000 structures on PES, which are then filtered to remove the redundant structures and refined using DFT calculations (see Section 2.2 below) to obtain accurate energy,

DOI: 10.1021/acscatal.8b03077
ACS Catal. 2018, 8, 9711−9721

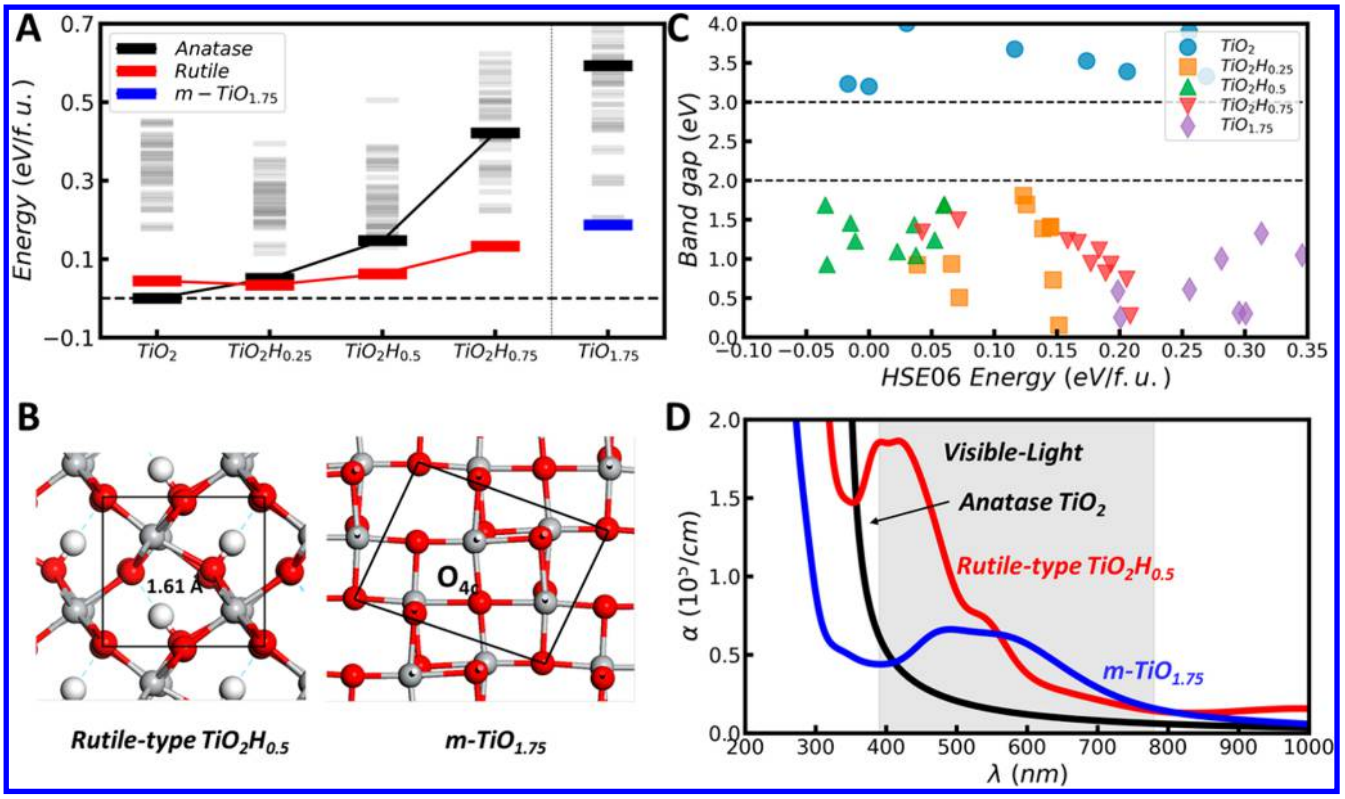

Figure 2. Properties for varied TiO_xH_y bulk phases after hydrogenation obtained from SSW-NN. (A) DFT energy spectrum for TiO_xH_y structures. All energies are with respect to the energy of anatase and a hydrogen molecule that are set as zero. (B) Identified most stable crystal structures at $TiO_2H_{0.5}$ and $TiO_{1.75}$ compositions. The dashed lines indicate the hydrogen bonds in the rutile-type $TiO_2H_{0.5}$. Ti, gray balls; O, red balls; H, white balls. (C) Band gaps of 10 lowest-energy structures for each composition (TiO_2, $TiO_2H_{0.25}$, $TiO_2H_{0.5}$, $TiO_2H_{0.75}$, and $TiO_{1.75}$) computed from the DFT HSE06 functional. (D) Optical absorption coefficient (α) for pure anatase TiO_2, the rutile-type $TiO_2H_{0.5}$, and the *m*-$TiO_{1.75}$ structures computed from the DFT HSE06 functional.

force, and stress. The final global data set contains around 140 000 structures (see Table S1).

2.1.b. NN PES Fitting. We are now ready to produce the TiO_xH_y NN potential using the global data set. Following our previous work,[24] the high-dimensional NN scheme introduced by Behler and Parinello[25] is utilized to construct NN potential, and the power-type structure descriptors are utilized to describe the geometrical environment of atoms. To pursue a high accuracy as desirable to differentiate the energy-degenerate configuration of TiO_xH_y, we have adopted a large set of structural descriptors, which contains 201 structure descriptors (SDs) for each element, i.e., 77 two-body SDs, 108 three-body SDs, and 16 four-body SDs, and compatibly, the network utilized is also large involving two hidden layers each with 50 neurons, equivalent to 38 103 network parameters in total. The input layer of NN is generated from the element-based power-type structure descriptors after rescaling to the (0, 1) range. Hyperbolic tangent activation functions were used for the hidden layers, while a linear transformation was applied to the output layer of all networks. The limited-memory Broyden−Fletcher−Goldfarb−Shanno (L-BFGS) method was used to simultaneously minimize the loss function to match DFT energy, force, and stress. The final energy and force criteria of the root-mean-square errors are 9.8 meV $atom^{-1}$ and 0.22 eV $Å^{-1}$, respectively. To demonstrate the accuracy of NN PES, we select 95 representative crystal/amorphous/surface structures, including $Ti_4O_8H_x$ (x = 1, 2, and 3) and the $Ti_{56}O_{112}H_{36}$ surface model, to compare the NN results with the DFT calculation results. It shows an acceptable average energy error of around 7.88 meV $atom^{-1}$. The details for the comparison results can be found in Table S2.

2.1.c. SSW Global Optimization Using NN PES. Utilizing the SSW-NN, we first explored the bulk phase space of TiO_2H_x and TiO_x with the 11−16 atoms per unit cell and the surface phase space of hydrogenated (112) surfaces ($Ti_{56}O_{112}H_x$). In each case, more than 10 000 minima on the potential energy surface are visited, which include a large variety of structures ranging from crystalline structures to amorphous structures. These minima on the PES are the inherent structures corresponding to the possible local structure patterns that occur when a material is cooled down rapidly. Then, all the low-energy structure candidates from SSW-NN exploration are verified by plane-wave DFT calculations with high-accuracy setups. Without being specifically mentioned, all energetics reported in this work refer to DFT results.

2.2. DFT Calculations and Optical Absorption Calculations. All DFT calculations were performed using plane-wave DFT code, VASP, where electron−ion interaction is represented by the projector augmented wave (PAW) pseudopotential.[26,27] The exchange functional utilized is the GGA-PBE[28] with the van der Waals corrections (zero damping DFT-D3 method of Grimme).[29] The kinetic energy cutoff utilized is 450 eV. The fully automatic Monkhorst−Pack *k*-mesh grid is generated with 15 times the reciprocal lattice vectors. The energy and force criteria for convergence of the electron density are set at 10^{-5} eV and 0.02 eV $Å^{-1}$, respectively. Moreover, the band gap is calculated by using the HSE06 hybrid functional.[30] The optical absorption property is calculated via the frequency-dependent

DOI: 10.1021/acscatal.8b03077
ACS Catal. 2018, 8, 9711−9721

dielectric matrix after the electronic ground state has been determined. More details about calculation details can be found in the SI.

3. RESULTS

3.1. Thermodynamics of TiO_xH_y Bulk Hydrogenation. Our investigation starts from the thermodynamic properties of bulk TiO_xH_y phases. To determine the most stable structure for each possible composition of the Ti:O:H ratio, we have utilized the SSW-NN global optimization to explore the PES of TiO_2, $TiO_2H_{0.25}$, $TiO_2H_{0.5}$, $TiO_2H_{0.75}$, and $TiO_{1.75}$ with the unit cell up to 16 atoms (the global PES are shown in Figure S1). Apparently, the formal valences of Ti of the investigated systems are among +3 to +4, which are consistent with XPS experiments.[31−33] More than 10 000 minima are obtained from SSW-NN for each composition. The most stable 50 minima were collected and refined using DFT, and the obtained energy spectra for these different TiO_xH_y structures are plotted in Figure 2. The relative stability of ΔE is calculated via eq 1 by referring to the energy of the common anatase phase.

$$\Delta E = E_{TiO_xH_y} - E_{TiO_2,A} - \frac{y + 2x}{2}E_{H_2} + (2 - x)E_{H_2O} \quad (1)$$

Here, $E_{TiO_xH_y}$, $E_{TiO_2,A}$, E_{H_2}, and E_{H_2O} are the energies of the TiO_xH_y structures, the perfect anatase phase, hydrogen gas, and water, respectively.

Figure 2 shows that (i) the most stable hydrogenated and deoxygenated TiO_2 structures in bulk turn to be the rutile-type and *m*-type (the details of *m*-type are shown below) structures, and (ii) the hydrogenated TiO_2 structures are generally more stable than the deoxygenated TiO_2. For pure TiO_2, the anatase phase is ∼0.06 eV per formula unit (eV fu^{-1}) more stable than the rutile phase, but the hydrogenated rutile-type structure, the global minimum phase after the hydrogenation, is more stable than the hydrogenated anatase phase by 0.02, 0.08, and 0.29 eV fu^{-1} at H:Ti = 0.25, 0.5, and 0.75, respectively. In fact, many other densely packed phases, e.g., TiO_2(II) phase, after hydrogenation are also more stable than the hydrogenated anatase.

We notice that the existence of H-bonding in the bulk for the hydrogenated TiO_2 plays important role in stabilizing these hydrogenated structures. We have counted the likely hydrogen bond (OH···OTi) length for all low-energy hydrogenated TiO_2H_x structures and found that more than 80% of structures have the length less than 1.8 Å (Figure S1), indicating the wide existence of typical H-bonding. This may well explain the stability of the hydrogenated rutile: each hydrogen atom can form one H-bond in the rutile-type TiO_2H_x phase. The H atoms bond with three coordinated O anions with the bond length of around 1.00 Å, driving the O anion away from the original equilibrium position in TiO_2 bulk (0.2−0.3 Å), and the final achieved H-bonding length is 1.60 Å. On the other hand, the anatase-type TiO_2H_x phase has essentially no H-bonding. This is due to the fact that the O−O distance in the anatase lattice is 3.78 Å, much longer than that in rutile (3.32 Å).

Going from the low to the H concentration, we note that the rutile-type TiO_2H_x at the high H concentration ($TiO_2H_{0.75}$) becomes significantly unstable (0.13 eV fu^{-1}), which suggest that the Ti^{3+} concentration higher than 50% in bulk would be thermodynamically highly unfavorable. In contrast, at the low H concentration, the hydrogenation of the bulk only induces a small energy cost as also found previously,[17] which opens the possibility for the hydrogenation to occur on surfaces/interfaces where the local structure is more flexible with low-coordinated sites.

Unlike the most stable hydrogenated phases that prefer the common rutile structure, the deoxygenated $TiO_{1.75}$ finds a new crystal phase for a global minimum. It possesses a monoclinic $C2/m$ symmetry (12), named as *m*-$TiO_{1.75}$, which is 0.41 eV fu^{-1} more stable than the anatase-type $TiO_{1.75}$ structure. Interestingly, there are in fact no visible O_v's in the *m*-$TiO_{1.75}$; all Ti cations are six-coordinated, the same as perfect anatase and rutile TiO_2, whereas one planar four-coordinated O atom (O_{4c}) per cell (11 atom $cell^{-1}$) appears. As a result, the volume of *m*-$TiO_{1.75}$ shrinks to 30.43 $Å^3$ fu^{-1} (anatase: 34.66 $Å^3$ fu^{-1}).

It should be mentioned that the planar O_{4c} appears to be a common structural feature for deoxygenated TiO_2 at the high O_v concentration (>4%). For example, using SSW-NN, we further investigated the global PES of $Ti_{12}O_{23}$ ($TiO_{1.92}$) per cell, starting from a different initial phase (anatase, rutile, etc.). Similarly, near the O_v, the phase undergoes reconstruction leading to the formation of the planar O_{4c} and the disappearance of O_v and Ti_{5c} (see Figure S2). This global minimum, basically an anatase phase with local reconstructions, is 0.07 eV fu^{-1} more stable than the anatase-type structure without reconstruction. Therefore, our results suggest that the deoxygenated TiO_2 tends not to have the commonly believed O_v, but prefers to form a new transformed dense oxide structure with planar O_{4c}.

It is also interesting for us to examine the electron structures of these TiO_xH_y structures and their optical absorption spectrum. The band gap and optical absorption spectrum from HSE06 functional calculations are plotted in Figure 2C,D. For pure TiO_2, they generally have a large bad gap (>3.0 eV) as expected from common knowledge. Indeed, the anatase TiO_2 exhibits the optical absorption only in the ultraviolet-light region (<400 nm). By contrast, the band gaps of TiO_2H_x and $TiO_{1.75}$ structures are much reduced to less than 2.0 eV, and consistently, the optical absorption coefficients for the rutile-type $TiO_2H_{0.5}$ and *m*-$TiO_{1.75}$ structures show large absorption at the visible-light region with the peak at 400−600 and 450−650 nm in the visible-light region, respectively. This implies that these crystals could be active photocatalysts under visible-light regions. However, we also note that the range of the absorption wavelength for rutile-type $TiO_2H_{0.25}$ and *m*-$TiO_{1.75}$ structures does not cover the whole visible-light region, especially only weak absorption at the long-wavelength region, which indicates that they are not the black color as observed for the amorphous TiO_2 in experiment.[4] The bulk calculations are not enough to rationalize the experimental findings on the color change upon the hydrogenation.

Our results from global PES exploration of bulk TiO_xH_y suggest that neither the hydrogenated TiO_2H_x nor the deoxygenated TiO_x phases can be more stable than pure TiO_2 phases. The bulk hydrogenation is thus highly thermodynamically hindered. In fact, the experiments show that after the hydrogenation the well-crystallized bulk with either anatase or rutile structure is reserved, and the significant structure change occurs dominantly on the surfaces of TiO_2 particles.

3.2. Thermodynamics of TiO_xH_y Surface Hydrogenation. Our next task is to study the hydrogenation process on the TiO_2 surface. Considering that the real anatase nanoparticles are often <20 nm and expose various facets, we utilize the SSW-NN method to explore the likely structures after hydrogenation, including (101), (001), (100), and (112) (see Figure 3), which

DOI: 10.1021/acscatal.8b03077
ACS Catal. 2018, 8, 9711−9721

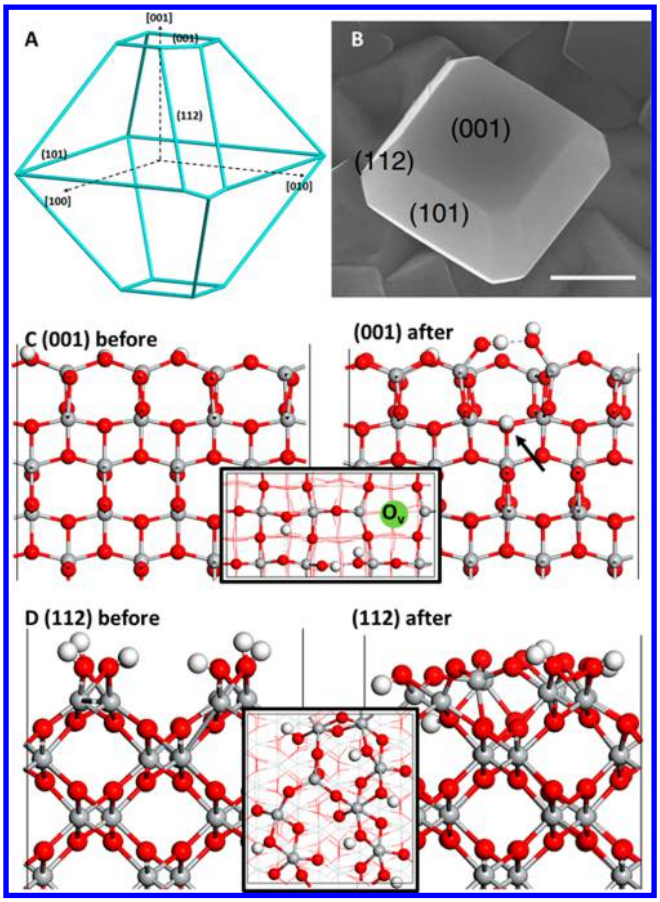

Figure 3. Reconstruction of common anatase surfaces in the presence of surface H atoms studied by SSW-NN PES exploration. (A) Typical decahedral morphology of the anatase particle. (B) The SEM picture is adapted from ref 34 with permission (Copyright 2014, Nature Publishing Group). (C, D) (001) and (112) surface before and after the surface reconstruction as induced by a high coverage of surface H.

are commonly available on anatase decahedron particles synthesized in the experiment.[34] The (101), (001), and (100) facets are terraces with low surface energies; the (112) facets, being 41.2° from (101), are the ridge separating two neighboring (101) facets which is identified as the phase transition facet of anatase-to-rutile (see Figure 3A,B).[22]

In the SSW-NN simulation, each surface slab contains at least 5 layers with more than 180 atoms (see Figure S3), and all atoms are allowed to relax. Initially, all H atoms are coordinated with the surface O_{2c} atoms with a surface coverage of a 0.75 monolayer (ML, with respect to surface Ti cations), abbreviated as TiO_2-0.75H (hereafter the x ML H or O_v covered TiO_2 surface follows the similar TiO_2-xH or TiO_2-xO_v notation). For the removal of the artificial dipole between slabs, H atoms are added on both sides. This high H surface coverage is to quickly screen the surfaces with the high reconstruction probability. For each surface, over 10 000 minima starting from the unreconstructed surface (i.e., having the Ti−O anatase lattice) are visited, from which the exothermic surface structures are collected and analyzed. We found that, among the four surfaces studied, two surface facets, (001) and (112), can undergo appreciable surface structure change that is exothermic. The structures of the surfaces before and after the reconstruction are summarized in Figure 3C,D.

For (001) facets, our SSW simulations show that 1/6 surface hydrogen atoms immerse into the bulk, sitting on the subsurface O_{3c} (as indicated by the arrow in Figure 3C), and more importantly, the surface Ti_{5c}−O_{2c}−Ti_{5c} bridge opens up by cleaving one of the Ti_{5c}−O_{2c} bonds, forming one standing OH group (Ti_{5c}−O_{2c}H) and one Ti_{4c} atom which is then saturated by another OH group, linking via the H-bonding between Ti−OH···HO−Ti. This second OH is formed by the hydrogenation and migration of another surface O_{2c} that originally acts as the bridge to connect two surface Ti_{5c} atoms. It thus leads to the formation of a surface O_v (see top view in Figure 3C). It should be mentioned that the opening of the Ti_{5c}−O_{2c}−Ti_{5c} bridge on the (001) surface has been observed in water adsorption via theories.[35−37] Our DFT calculations show that the reconstructed surface can be 0.56 eV per (4 × 2) surface more stable than the unreconstructed surface. However, the (001) reconstruction mainly involves the surface oxygen migration with little change in Ti cation positions. No obvious surface amorphization is observed on the (001) surface after hydrogenation.

By contrast, for the (112) facets, a complex surface structural pattern features a diversity of Ti coordination environments, including Ti_{4c}, Ti_{5c}, and Ti_{6c}. As shown in Figure 3D, nearly half of Ti atoms on the first layer have changed their position. In particular, 25% Ti_{5c} cations become Ti_{4c} cations due to their significant upshift from the surface, and another 25% Ti_{5c} cations collapse into the subsurface layer forming Ti_{6c} cations. On the final reconstructed surface, the Ti−O bond length has a wide distribution, from 1.80 to 2.2 Å, as compared to 1.9−2.1 Å on the unreconstructed (112) surface. Obviously, the reconstructed (112) surface becomes amorphous by completely losing the original anatase bonding patterns. Our results suggest that the surface hydrogenation may initiate from the anatase (112) ridged surface, and the exact H coverage will be determined in the next section.

3.3. Thermodynamic Phase Diagram. By focusing on the anatase (112) surface, we have performed a series of SSW-NN simulations with different H coverages aiming to map out the realistic experimental conditions, i.e., at different temperature/pressures.

Figure 4A shows the energy profile of the hydrogenated (112) surface at different surface H coverages with (orange curve) and without (blue curve) the surface reconstruction. The reaction energy is computed using eq 1 according to the formula $TiO_2(112) + x0.5H_2 \rightarrow TiO_2$-$x$H by referring to the unreconstructed TiO_2 surface. As shown, at low hydrogen coverage (≤0.19 ML), the (112) surface remains intact with all added hydrogen sitting on the surface O_{2c}. Above 0.19−0.31 ML, the surface starts to reconstruct, which is driven by thermodynamics. The highest exothermicity occurs at the hydrogen coverage at 0.69 ML. This is in sharp contrast to the unreconstructed surface, which is 3.64 eV per (4 × 2) surface less stable than the reconstructed TiO_2-0.69H surface. Many different reconstructed surfaces can be observed with energy between the unreconstructed and the most stable reconstructed surface (Figure S4). Above 0.69 ML, the surface hydrogenation becomes less favorable, indicating that the new H atoms arriving on the surface are in fact less stable than the gas phase H_2. The reconstruction helps the surface to accommodate more hydrogen atoms (~0.69 ML), while the unreconstructed (112) surface can only accommodate maximally 0.19 ML hydrogen coverage when the H atom adsorption is exothermic.

DOI: 10.1021/acscatal.8b03077
ACS Catal. 2018, 8, 9711−9721

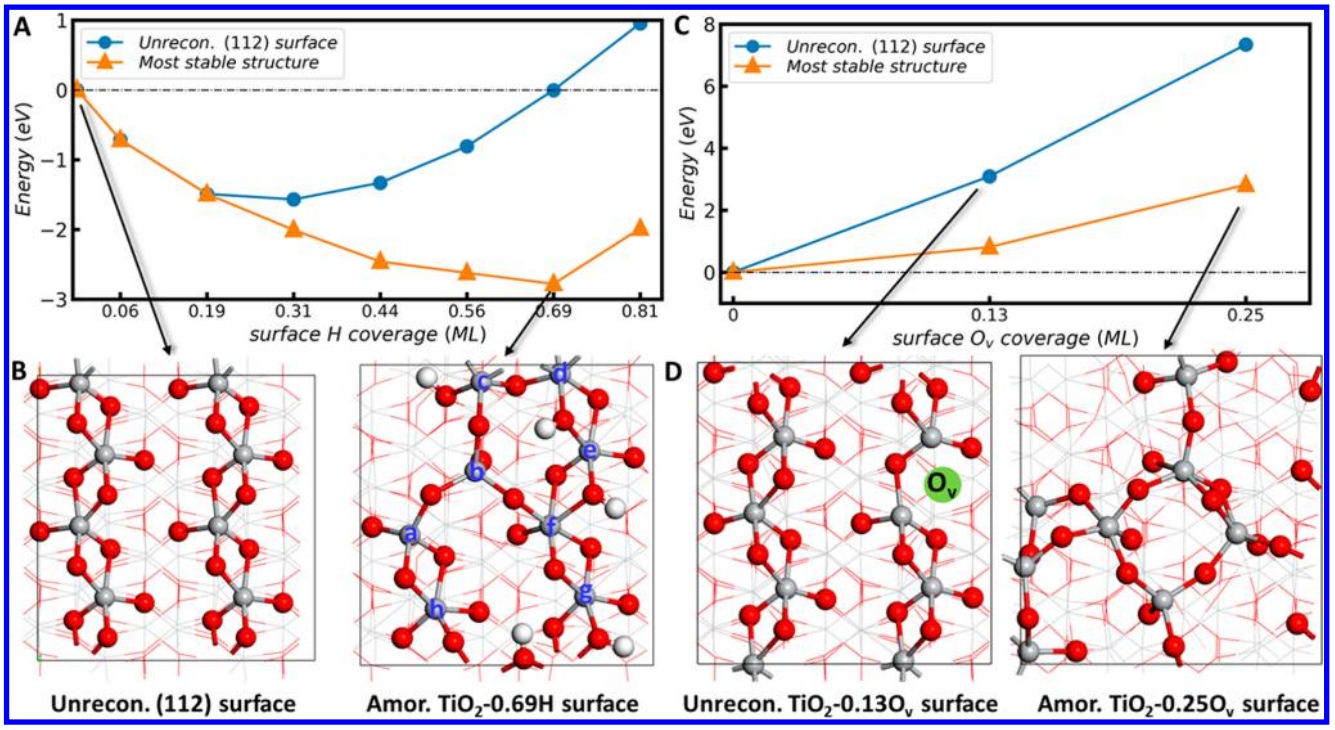

Figure 4. Energetics and structures for TiO_2 (112) after hydrogenation treatment. (A, B) Relative energy and selected structures for the H covered (112), TiO_2-xH with the coverage x from 0 to 0.81 ML. (C, D) Relative energy and selected structures for the (112) with O vacancies, TiO_2-$x$$O_v$ with the O_v coverage x from 0 to 0.25 ML. All energetics are from DFT calculations and with respect to the energy of pristine (112) and the H_2 molecule. These most stable structures at different compositions are identified from the SSW-NN global search, with more than 10 000 minima visited for each composition. As shown in parts B and D, the reconstructed surfaces after hydrogenation become amorphous with the appearance of various Ti coordinations. For the (4 × 2) (112) surface studied, there are two Ti_{4c}, four Ti_{5c}, and two Ti_{6c} in amorphous TiO_2-0.69H; four Ti_{4c} and four Ti_{5c} in amorphous TiO_2-0.25O_v.

We now focus on the local geometry of the reconstructed TiO_2-0.69H surface. As shown in Figure 4B, the interaction between the TiO_2 host and H atoms gives rise to large structural distortions, leading the generation of an amorphous shell featuring a diversity of Ti coordination environments (Ti_{4c}, site a, b; Ti_{5c}, site c, e, g, h; and Ti_{6c}, site d, f). The shortest distance of O_{2c}−O_{2c} is only 2.7 Å, being 0.3 Å shorter than that on unreconstructed (112) surface.

Similarly, we investigate the deoxygenated (112) surface using SSW-NN simulation where the initial surface O_v coverages are set as 0.13 and 0.25 ML, which are equivalent to TiO_2 with 0.26 and 0.50 ML H coverage, respectively. At these H coverages, the reconstructed surface should be energetically more favorable. The reaction energy is computed using eq 1 according to the formula $TiO_2(112) + xH_2 \rightarrow TiO_2\text{-}xO_v + xH_2O$ by referring to the unreconstructed TiO_2 (112) surface. The energy profile is shown in Figure 4C. Similarly, the SSW simulations for the deoxygenated (112) surfaces show that the surface reconstruction can dramatically stabilize the TiO_2-$x$$O_v$ (112) surface. The identified most stable reconstructed structure for TiO_2-$x$$O_v$ with 0.13 (0.25) ML O_v coverage is 2.3 (4.5) eV more stable than the unreconstructed surfaces. The deoxygenated reconstructed surfaces, despite the lack of H atoms, show structural similarity with the hydrogenated reconstructed surfaces, which have an amorphous shell with both Ti_{4c} and Ti_{5c} cations (Figure 4D). It should be emphasized that while these amorphous TiO_2-$x$$O_v$ surfaces are more stable than the unreconstructed surface, they are in fact energetically less favorable compared to the perfect TiO_2. As DFT energies correspond to the Helmholtz free energy at 0 K (without zero-point energy), this suggests that the deoxygenation cannot occur at low temperatures, as indeed observed in experiment.[38,39]

With the DFT energetics of various TiO_xH_y structures, ranging from bulk to surfaces, we are now in the position to establish the phase diagram of TiO_2 material under different hydrogenation temperatures and hydrogen pressures. To do so, the *ab initio* thermodynamics analyses have been performed to determine the stability of TiO_2 material where the above-mentioned formulas are used to compute the free energy change as a function of temperature and H_2 partial pressure. The Gibbs free energy change is based on DFT reaction energies with the zero-point energy, entropy, and enthalpy corrections. More calculation details can be found in the SI. The phase diagram of TiO_xH_y under hydrogenation conditions is plotted in Figure 5, where three distinct regions can be identified. The experimental data are also indicated in Figure 5 for comparison. The three regions are elaborated as follows.

Region I is unreconstructed TiO_xH_y (with Ti−O anatase lattice). This zone appears as a small white trigonal zone at the temperature of around 220 °C and H_2 pressure of around 0.03 bar. In this region, the presence of O_v or surface H, if present, must be low in coverage and thus does not reconstruct the surface or the bulk.

Region II is the amorphous TiO_2-xH surface. This zone appears as a large cyan zone with the temperature and pressure range from 200 °C, 0.1 bar, to 300 °C, 70 bar. While being amorphous, the surface may have different hydrogen coverage depending on temperature and H_2 pressure. The low temperature and high H_2 pressure lead to the high hydrogen coverages. The hydrogenation of bulk occurs only at very high H_2 pressure

DOI: 10.1021/acscatal.8b03077
ACS Catal. 2018, 8, 9711−9721

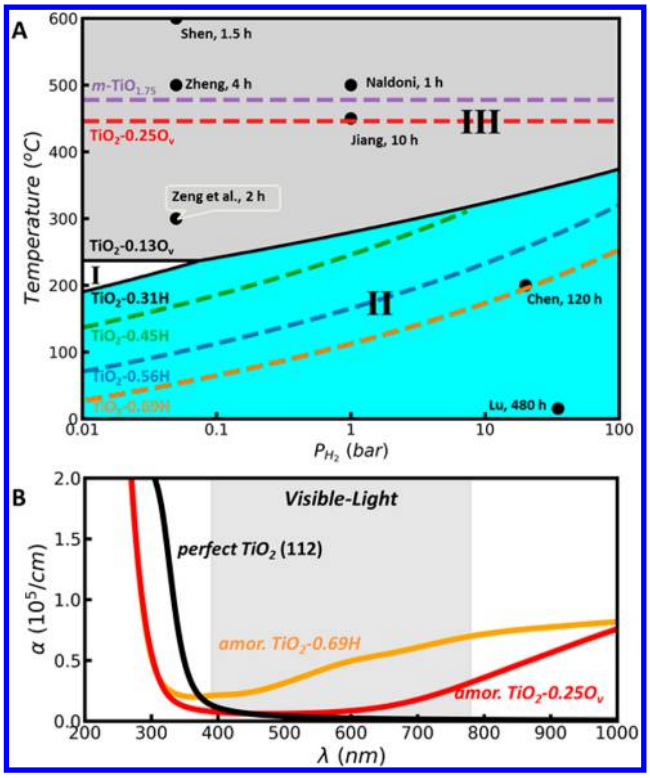

Figure 5. (A) Thermodynamic phase diagram of TiO_2 in contact with H_2. (B) Optical absorption spectrum for amorphous TiO_2 surfaces. In part A, three regions are colored, representing the unreconstructed $TiO_{2-x}H_y$ structures (white zone), the deoxygenated amorphous bulk and surfaces (gray zone), and the amorphous H covered surfaces (cyan zone). The experimental data are indicated by black dots, which are all located in the amorphous regions (gray or cyan zone). The dashed lines in the figure represent the equilibrium lines between neighboring phases at varied compositions. The phase diagram is computed from the free energy data based on DFT energetics by using eq 1. The water pressure is assumed to be 100 ppm relative to hydrogen pressure.

(0 °C, 1000 bar), indicating that the bulk hydrogenation is thermodynamically hindered.

We note that the maximum hydrogen concentration can reach 0.69 ML at the hydrogenation condition of 200 °C and 20 bar hydrogen pressure. As reported by Chen et al., black TiO_2 contains about 0.25 wt % hydrogen as detected by gravimetric hydrogen sorption−desorption measurement at 200 °C.[1] According to their measured nanoparticle size (∼8 nm) and the amorphous shell thickness (∼1 nm), we estimate roughly that the H coverage in their samples is around 0.4 ML on the amorphous surface (see Figure S5). The lower H coverage from experiment compared to theory may come from a number of possible sources, e.g., the slow kinetics of hydrogenation in experiment, or the theoretical estimation taken from the thermodynamic data of (112) surface hydrogenation. Nevertheless, the 0.4 ML H coverage is already in the amorphous region II as predicted in Figure 5 and is much larger than that which can be taken by the pristine TiO_2 surfaces. Moreover, few hydrogenation experiments were carried out at the low temperatures, which should mainly be due to the slow kinetics of surface reconstruction and thus a long induction period for catalyst preparation. For example, the TiO_2 hydrogenation by Lu et al. takes 480 h at 25 °C and 70 bar H_2 pressure.[6]

Region III is the amorphous TiO_2-xO_v surface and deoxygenated bulk phase. This zone appears as a large gray zone at temperatures larger than ∼300 °C. The H_2 pressure at such high temperatures becomes irrelevant to the thermodynamically stable structure since H_2 would strongly prefer to form H_2O at these conditions. Importantly, the bulk phase equilibrium line (TiO_2 to $TiO_{1.75}$) from theory appears at the temperature of 480 °C. It indicates that the high-temperature hydrogenation may even introduce new deoxygenated bulk phases.

Our predicted phase diagram covers a number of experiments performed under high temperatures but with very different hydrogen pressure conditions, e.g., H_2 plasma, 5% H_2/Ar flow, and 70 bar H_2.[3,7,40,41] The O_v is widely observed in their samples, which are consistent with the theoretical prediction that at the high temperatures all TiO_2 materials tend to have the deoxygenated surfaces and bulk. Different from the hydrogenation at low temperature with slow kinetics, high-temperature hydrogenations show much faster kinetics which allows the hydrogenation to be fulfilled with only a few hours (<10 h).[3,11,42−44]

As the black color of hydrogenated titania is a key observation from experiment, it is necessary for us to verify the optical absorption for the amorphous structures predicted from theory. In Figure 5B, we show the calculated optical absorption coefficients of the perfect TiO_2 (112) surface, the amorphous TiO_2-$0.25O_v$ surface, and the amorphous TiO_2-0.69H surface by using the hybrid HSE06 functional. As shown, the perfect TiO_2 (112) surface exhibits the major optical absorption in the ultraviolet-light region (black curve), showing the white color. The amorphous TiO_2-$0.25O_v$ surface has a large optical absorption in the near-infrared-light region (>700 nm, red curve), implying the appearance of a blue color. By contrast, the amorphous TiO_2-0.69H surface covers the whole visible-light region and has a particular large absorption at long-wavelength regions (orange curve). Our results therefore confirm that the presence of a high coverage of H atoms on the amorphous titania is an essential condition for the material to exhibit the black color.

3.4. HER Activity on Amorphous Hydrogenated TiO_2.

We are now in the position to search for the active sites of the HER on amorphous TiO_2 surfaces after hydrogenation. Because of the structural similarity between hydrogenated surfaces and deoxygenated surfaces, e.g., amorphous structure with similar Ti and O coordination, we mainly focus on the hydrogenated surfaces for the HER, i.e., amorphous TiO_2-0.69H as shown in Figure 4B, since the H coverage is already built up. The H coupling reaction pathways of the HER ($2H^* \rightarrow H_2$) on all the likely sites have been investigated, which is known to be the rate-limiting step for the HER on oxides.[45,46] The lowest-energy reaction pathways via two different mechanisms are plotted in Figure 6A, i.e., via the OH/OH coupling (the red curve) and the TiH/OH coupling (orange curve). The H coupling reaction on the unreconstructed (112) surface is also studied and shown in Figure 6A (black curve) for reference.

On the unreconstructed (112) surface with one preadsorbed H atom on the O_{2c} atom, the second hydrogen atom adsorbs on the neighboring O_{2c} site. This adsorbed H atom is slightly exothermic by 0.15 eV with respect to the standard hydrogen electrode condition, ($H^+ + e^- \rightarrow H_2$ at pH = 0 and H_2 pressure 1 bar). The presence of TiH hydride species, i.e., H on Ti_{5c}, is thermodynamically unlikely, which is endothermic by at least 1.43 eV. Then, the HER proceeds by the H coupling starting from two OH groups. Because of the long geometrical distance between two neighboring $O_{2c}H$ (H−H distance is 3.6 Å at the

DOI: 10.1021/acscatal.8b03077
ACS Catal. 2018, 8, 9711−9721

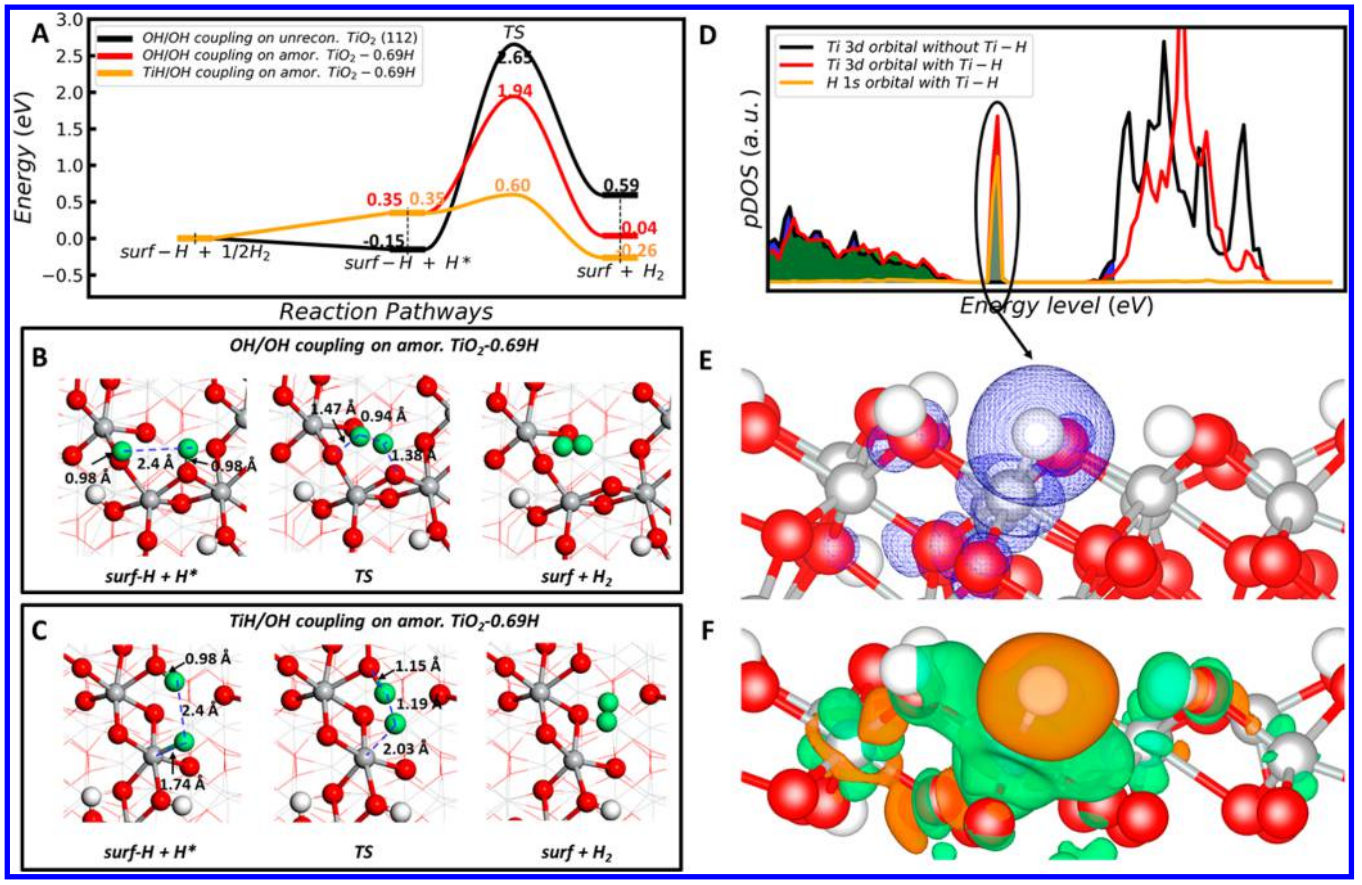

Figure 6. Mechanism and energetics for H coupling in the HER on the amorphous TiO_2-0.69H surface. (A) Energetic profiles of H coupling via the OH/OH coupling and the TiH/OH coupling mechanisms on the pristine (112) surface and amorphous TiO_2-0.69H. (B, C) Reaction snapshot from the top view of (112). Ti, gray balls; O, red balls. H, white balls (H in reaction, green ball). (D) Projected density of states (pDOS) of the Ti 3d orbital and H 1s orbital (in TiH hydride) before and after the formation of TiH hydride species on amorphous TiO_2-0.69H. The filled regions represent the occupied states. (E) Charge density (the square of wave function) contour plot for the TiH bonding state on amorphous TiO_2-0.69H. (F) Charge density difference contour plot before and after the formation of TiH hydride on amorphous TiO_2-0.69H. The green and orange colors indicate the decrease and increase in the electron density, respectively. The 3D isosurface value is set as 0.003 e $Å^{-3}$.

initial state), the reaction has a very high barrier of 2.8 eV. This may not be surprising since a similar high barrier was also reported for the TiO_2 (101) surface for which the H_2 recombinative desorption via the OH/OH mechanism is thermodynamically favorable but with a large energy barrier (1.52−2.2 eV).[45−47]

On the amorphous TiO_2-0.69H surface, similarly we first examined the OH/OH coupling mechanism. By mapping out all the likely binding sites, we found that the arrival of new H atoms on O_{2c} is endothermic by ∼0.35 eV, which is expected since the 0.69 ML H coverage is the most favorable coverage thermodynamically. At this high coverage, the reaction via the OH/OH coupling remains highly difficult with a barrier of at least 1.6 eV, despite a shorter H−H distance (2.40 Å) at the initial state compared to that of the unreconstructed TiO_2−$H_{0.13}$ (112) surface (Figure 6A,B).

Instead, we found that on the amorphous TiO_2-0.69H surface a low-energy reaction channel opens, where the H coupling is much promoted via a new TiH/OH coupling mechanism. Unlike that on the unreconstructed surface, the presence of a TiH hydride species is much favored on the amorphous TiO_2-0.69H. From our calculations, there are at least 3/8 Ti sites (site a, e, and g in Figure 4B) that become available to form transient Ti−H hydride species on the surface. The formation energies, although still positive, are only 0.35−0.5 eV (Figure S6). The Ti−H bond length is around 1.70−1.80 Å, and the shortest H−H distance between TiH and OH is ∼2.4 Å (see Figure 6C). These Ti−H hydride species, once formed, are ready to react with the neighboring H (on O_{2c}). At the TS, the Ti−H bond is elongated to 2.03 Å, and the H−H distance is reduced to 1.19 Å. This coupling step has a very low-energy barrier of 0.25 eV. With the overall barrier of 0.60 eV, the TiH/OH coupling pathway for hydrogen production is ∼24 orders of magnitude faster than the direct OH/OH coupling, indicating that the TiH/OH mechanism is the only likely reaction for the HER on amorphous TiO_2 material.

By analyzing the electronic structures before and after the forming of TiH species, we further investigate why the TiH hydride species is much stabilized on amorphous TiO_2-0.69H. In Figure 6D, we plot the 3d orbital projected density of states (pDOS) of the Ti atom before and after its coordination with the arriving H (TiH hydride) on the amorphous TiO_2-0.69H (black and red curves). For reference, the 1s orbital pDOS for the H in TiH species is also plotted (orange curve). We find that before TiH formation excess electrons are present near the conduction band minimum (CBM), which belong to the occupied Ti 3d orbitals and suggest the reduction of Ti^{4+} to Ti^{3+} due to the presence of surface H atoms that bond with lattice O (thus they are proton-like). Once the TiH hydride species forms, the electrons on the Ti 3d orbital disappear, and a new peak emerges

DOI: 10.1021/acscatal.8b03077
ACS Catal. 2018, 8, 9711−9721

in the band gap. This peak is assigned to the covalent bonding between the Ti 3d orbital and H 1s orbital to form the 3d−1s hybrid orbital (Figure 6E) as it has a large component on both Ti and H pDOS. The formation of TiH species induces the electron transfer from the high-energy-level Ti 3d orbital to this low-energy-level 3d−1s bonding orbital.

The charge density difference contour plot shown in Figure 6F confirms the electron transfer direction in the formation of TiH species, which is constructed by subtracting the total electron density of the system before and after the TiH formation, $\Delta\rho = \rho[\text{H-TiO}_2\text{-0.69H}] - \rho[\text{TiO}_2\text{-0.69H}] - \rho[\text{H}]$. Figure 6F shows a significant local electron transfer from the Ti atom to H atom, leading to the electron density accumulation on the H atom but depletion on the Ti atom. It is also noted that the neighboring OH group is also polarized with the further decrease of the electron density on the H, suggesting that the presence of the neighboring OH also helps to stabilize the TiH species. This is the key for the low barrier of H coupling on the amorphous TiO_2-0.69H, where the negatively charged H on TiH can react with the neighboring protons on lattice O.

Considering that the neighboring OH group helps to stabilize TiH hydride species, we have further examined the influence of the neighboring OH group on the TiH stability by gradually removing the neighboring H on lattice O and computing the formation energy of TiH species. This shows that the formation of TiH becomes more endothermic with the decrease of the neighboring OH group (corresponding to H coverage). It is the least endothermic, 0.35 eV at TiO_2-0.69H, and increases to 0.51 eV at TiO_2-0.62H, and 0.88 eV at TiO_2-0.56H. Similar phenomena can in fact be observed on the unreconstructed (112) surface with the increase of H coverage (Figure S7). Therefore, a high H coverage that becomes thermodynamically favorable on the amorphous TiO_2 surface is vital to produce the transient TiH hydride for the HER.

4. DISCUSSION

Our results suggest that the TiH species that are available only on the amorphous TiO_2 surfaces are critical to the HER activity. It is therefore interesting to discuss the previous findings on the TiH species on different TiO_2 surfaces. On crystalline TiO_2, it is generally known that the TiH hydride species is not present at ambient conditions. Previous theoretical calculations[46] and also this work show that the TiH hydride species on anatase TiO_2 surfaces are very unstable and thus migrate readily to neighboring lattice O_{2c}. Indeed, TiH hydride on crystalline TiO_2 surfaces is never observed in experiment. On amorphous hydrogenated TiO_2 surfaces, the recent XPS evidence from several experiments seems to support the presence of TiH, although its connection with HER activity was not established. For example, a shoulder peak at 457.3 eV in the Ti 2p XPS spectrum was observed and attributed to the surface TiH hydride species on different experimental samples, such as hydrogenated TiO_2 nanosheets,[32] the hydrogenated TiO_2 nanowire microspheres,[41] and the hydrogenated TiO_2 nanocrystals.[48]

Our analyses further demonstrate that the high surface H coverage is the prerequisite for the formation of TiH hydride species. As shown in Figure 4A, the unreconstructed (112) surface can only accommodate maximally 0.19 ML H coverage until the H atom adsorption becomes endothermic. It is no wonder that TiH hydride species is absent on the crystalline surfaces. On the other hand, the structural amorphization under high H_2 pressure increases the H coverage up to ∼0.69 ML. Therefore, how to efficiently promote surface amorphization for crystalline TiO_2 is a key challenge in experiment.

By comparing the ridged TiO_2 (112) surface with the other low Miller index surfaces, e.g., (101), (001), and (100), for which it is hard to be amorphous, we find that the TiO_2 (112) surface with ridges and valleys has a large open spaces to allow Ti cation migration. This helps to release the surface tension caused by the breaking of lattice Ti−O bonds due to the formation of OH groups on the surface. On the basis of this geometrical fact, we therefore propose TiO_2 material candidates that may accelerate surface amorphization. (i) For smaller nanocrystals, the surface area of nanocrystals increase sharply with the reduction of the size, and therefore, smaller nanocrystals should have much faster hydrogenation kinetics. (ii) For a high concentration of structural defects, this may be introduced by heterogeneous junctions; e.g., the rutile and anatase biphase junction is not structurally coherent and thus may introduce open space at the phase boundary.[22] (iii) For a high concentration of (112) ridged surfaces, such TiO_2 nanocrystals can be synthesized by using special synergistic capping agents of organic citric acid and inorganic hydrofluoric acid.[34] (iv) For hollow cage TiO_2 materials, several TiO_2 crystals have micropores with open channels 3−7 Å, e.g., ramsdellite-like TiO_2(R),[49,50] hollandite-like TiO_2(H),[51] and the recently theoretically predicted TiO_2(TB) phases.[52] We note that no hydrogenation experiment has been reported on these materials, and thus, further experimental studies along the line to create open surfaces may facilitate the development of new black TiO_2 catalysts for the HER.

5. CONCLUSION

By using global sampling and machine learning potential, this work establishes the phase diagram of TiO_2 in contact with H_2 that leads to the first identification of the active site on amorphous surfaces for the photocatalytic HER. We show that, among a variety of common anatase surfaces, the ridged anatase (112) is the key surface that initializes the surface amorphization, and the amorphous surface can hold up to 0.69 ML surface H, which is substantially higher than the crystalline surface (below 0.19 ML). The high H coverage opens a new reaction channel for the HER via TiH hydride reacting with the surface OH. This finding of TiH hydride on hydrogenated amorphous TiO_2 is exceptional since it is known to be highly unstable on crystalline TiO_2 both in theory and from experiment. We demonstrate that the stability of TiH hydride can be attributed to the electron transfer from the reduced Ti cation and the strong polarization of neighboring OH groups, both being only available at high H coverage. Our results provide concrete evidence on the new surface species and new reaction channels that emerge on amorphous materials and thus should benefit the further reaction design via surface amorphization. Our detailed results are outlined as follows.

(i) TiO_2 bulk hydrogenation is thermodynamically hindered from DFT energetics of the global PES data set. Neither the hydrogenated TiO_2H_x nor the deoxygenated TiO_x bulk phases can be energetically more stable than pure TiO_2 phases.

(ii) Among a variety of common anatase surfaces, (101), (001), (100), and (112) facets, only the ridged anatase (112) can become amorphous after hydrogenation.

(iii) The theoretical phase diagram of TiO_2 in contact with H_2 is established, which shows two major stable regions, the

DOI: 10.1021/acscatal.8b03077
ACS Catal. 2018, 8, 9711−9721

amorphous TiO_2-xH surface at low temperatures (<250 °C), and the deoxygenated amorphous bulk/surfaces at high temperatures (>300 °C).

(iv) The H coverage at 0.69 ML on anatase (112) creates the thermodynamically most stable amorphous surface, TiO_2-0.69H. From optical spectrum calculations, this amorphous layer exhibits the black color. The amorphous TiO_2-$x$$O_v$ surface, by contrast, shows a blueish color.

(v) The surface amorphization increases markedly the ability to accommodate a high coverage of atomic hydrogen, which allows for the formation of the transient TiH hydride that is the key species for the catalytic HER. The HER follows the TiH coupling with the OH mechanism with an overall barrier only 0.60 eV.

■ ASSOCIATED CONTENT

Supporting Information

The Supporting Information is available free of charge on the ACS Publications website at DOI: 10.1021/acscatal.8b03077.

Additional details on calculation methods; energy comparison between DFT and NN potential; H-bonding distribution results; structures of m-$TiO_{1.92}$; different surface models for hydrogenation; surface H coverage estimate; phonon density of states; TiH formation energy on different active sites; and atomic XYZ positions for local minima of TiO_xH_y (PDF)

■ AUTHOR INFORMATION

Corresponding Author

*E-mail: zpliu@fudan.edu.cn.

ORCID

Si-Da Huang: 0000-0002-0055-1510

Zhi-Pan Liu: 0000-0002-2906-5217

Notes

The authors declare no competing financial interest.

■ ACKNOWLEDGMENTS

This work was supported by the National Key Research and Development Program of China (2018YFA0208600), and National Science Foundation of China (21573149, 21533001, 91745201).

■ REFERENCES

(1) Chen, X.; Liu, L.; Peter, Y. Y.; Mao, S. S. Increasing Solar Absorption for Photocatalysis with Black Hydrogenated Titanium Dioxide Nanocrystals. *Science* **2011**, *331*, 746−750.

(2) Hu, Y. H. A. Highly Efficient Photocatalyst—Hydrogenated Black TiO_2 for the Photocatalytic Splitting of Water. *Angew. Chem., Int. Ed.* **2012**, *51*, 12410−12412.

(3) Naldoni, A.; Allieta, M.; Santangelo, S.; Marelli, M.; Fabbri, F.; Cappelli, S.; Bianchi, C. L.; Psaro, R.; Dal Santo, V. Effect of Nature and Location of Defects on Bandgap Narrowing in Black TiO_2 Nanoparticles. *J. Am. Chem. Soc.* **2012**, *134*, 7600−7603.

(4) Chen, X.; Liu, L.; Huang, F. Black titanium dioxide (TiO_2) nanomaterials. *Chem. Soc. Rev.* **2015**, *44*, 1861−1885.

(5) Chen, X.; Shen, S.; Guo, L.; Mao, S. S. Semiconductor-Based Photocatalytic Hydrogen Generation. *Chem. Rev.* **2010**, *110*, 6503−6570.

(6) Lu, H.; Zhao, B.; Pan, R.; Yao, J.; Qiu, J.; Luo, L.; Liu, Y. Safe and Facile Hydrogenation of Commercial Degussa P25 at Room Temperature with Enhanced Photocatalytic Activity. *RSC Adv.* **2014**, *4*, 1128−1132.

(7) Jiang, X.; Zhang, Y.; Jiang, J.; Rong, Y.; Wang, Y.; Wu, Y.; Pan, C. Characterization of Oxygen Vacancy Associates within Hydrogenated TiO_2: a Positron Annihilation Study. *J. Phys. Chem. C* **2012**, *116*, 22619−22624.

(8) Chen, X.; Liu, L.; Liu, Z.; Marcus, M. A.; Wang, W.-C.; Oyler, N. A.; Grass, M. E.; Mao, B.; Glans, P.-A.; Peter, Y. Y. Properties of Disorder-Engineered Black Titanium Dioxide Nanoparticles through Hydrogenation. *Sci. Rep.* **2013**, *3*, 1510.

(9) Wang, Z.; Yang, C.; Lin, T.; Yin, H.; Chen, P.; Wan, D.; Xu, F.; Huang, F.; Lin, J.; Xie, X. Visible-Light Photocatalytic, Solar Thermal and Photoelectrochemical Properties of Aluminium-Reduced Black Titania. *Energy Environ. Sci.* **2013**, *6*, 3007−3014.

(10) Liu, N.; Schneider, C.; Freitag, D.; Hartmann, M.; Venkatesan, U.; Müller, J.; Spiecker, E.; Schmuki, P. Black TiO_2 Nanotubes: Cocatalyst-free Open-Circuit Hydrogen Generation. *Nano Lett.* **2014**, *14*, 3309−3313.

(11) Shin, J.-Y.; Joo, J. H.; Samuelis, D.; Maier, J. Oxygen-Deficient $TiO_{2-\delta}$ Nanoparticles via Hydrogen Reduction for High Rate Capability Lithium Batteries. *Chem. Mater.* **2012**, *24*, 543−551.

(12) Zhu, G.; Lin, T.; Lü, X.; Zhao, W.; Yang, C.; Wang, Z.; Yin, H.; Liu, Z.; Huang, F.; Lin, J. Black Brookite Titania with High Solar Absorption and Excellent Photocatalytic Performance. *J. Mater. Chem. A* **2013**, *1*, 9650−9653.

(13) Selcuk, S.; Zhao, X.; Selloni, A. Structural Evolution of Titanium Dioxide during Reduction in High-Pressure Hydrogen. *Nat. Mater.* **2018**, DOI: 10.1038/s41563-018-0135-0.

(14) Zhu, H.; Qin, Z.; Shan, W.; Shen, W.; Wang, J. Pd/CeO_2−TiO_2 Catalyst for CO Oxidation at Low Temperature: a TPR Study with H_2 and CO as Reducing Agents. *J. Catal.* **2004**, *225*, 267−277.

(15) Watanabe, S.; Ma, X.; Song, C. Characterization of Structural and Surface Properties of Nanocrystalline TiO_2− CeO_2 Mixed Oxides by XRD, XPS, TPR, and TPD. *J. Phys. Chem. C* **2009**, *113*, 14249−14257.

(16) Wang, G.; Wang, H.; Ling, Y.; Tang, Y.; Yang, X.; Fitzmorris, R. C.; Wang, C.; Zhang, J. Z.; Li, Y. Hydrogen-Treated TiO_2 Nanowire Arrays for Photoelectrochemical Water Splitting. *Nano Lett.* **2011**, *11*, 3026−3033.

(17) Liu, L.; Peter, Y. Y.; Chen, X.; Mao, S. S.; Shen, D. Hydrogenation and Disorder in Engineered Black TiO_2. *Phys. Rev. Lett.* **2013**, *111*, 065505.

(18) Large Scale Atomic Simulation with Neural Network Potential. www.lasphub.com.

(19) Shang, C.; Liu, Z.-P. Stochastic Surface Walking method for Structure Prediction and Pathway Searching. *J. Chem. Theory Comput.* **2013**, *9*, 1838−1845.

(20) Zhang, X.-J.; Shang, C.; Liu, Z.-P. From Atoms to Fullerene: Stochastic Surface Walking Solution for Automated Structure Prediction of Complex Material. *J. Chem. Theory Comput.* **2013**, *9*, 3252−3260.

(21) Guan, S.-H.; Zhang, X.-J.; Liu, Z.-P. Energy Landscape of Zirconia Phase Transitions. *J. Am. Chem. Soc.* **2015**, *137*, 8010−8013.

(22) Zhu, S.-C.; Xie, S.-H.; Liu, Z.-P. Nature of Rutile Nuclei in Anatase-to-Rutile Phase Transition. *J. Am. Chem. Soc.* **2015**, *137*, 11532−11539.

(23) Li, Y.-F.; Zhu, S.-C.; Liu, Z.-P. Reaction Network of Layer-to-Tunnel Transition of MnO_2. *J. Am. Chem. Soc.* **2016**, *138*, 5371−5379.

(24) Huang, S.-D.; Shang, C.; Zhang, X.-J.; Liu, Z.-P. Material Discovery by Combining Stochastic Surface Walking Global Optimization with a Neural Network. *Chem. Sci.* **2017**, *8*, 6327−6337.

(25) Behler, J. Representing Potential Energy Surfaces by High-Dimensional Neural Network Potentials. *J. Phys.: Condens. Matter* **2014**, *26*, 183001−1830024.

(26) Blöchl, P. E. Projector Augmented-Wave Method. *Phys. Rev. B: Condens. Matter Mater. Phys.* **1994**, *50*, 17953−17979.

(27) Kresse, G.; Joubert, D. From Ultrasoft Pseudopotentials to the Projector Augmented-Wave Method. *Phys. Rev. B: Condens. Matter Mater. Phys.* **1999**, *59*, 1758−1775.

(28) Perdew, J. P.; Burke, K.; Ernzerhof, M. Generalized Gradient Approximation Made Simple. *Phys. Rev. Lett.* **1996**, *77*, 3865−3868.

DOI: 10.1021/acscatal.8b03077
ACS Catal. 2018, 8, 9711−9721

(29) Grimme, S.; Antony, J.; Ehrlich, S.; Krieg, H. A Consistent and Accurate *ab initio* Parametrization of Density Functional Dispersion Correction (DFT-D) for the 94 Elements H-Pu. *J. Chem. Phys.* **2010**, *132*, 154104.
(30) Heyd, J.; Scuseria, G. E.; Ernzerhof, M. Hybrid Functionals Based on a Screened Coulomb Potential. *J. Chem. Phys.* **2003**, *118*, 8207−8215.
(31) Yu, X.; Kim, B.; Kim, Y. K. Highly Enhanced Photoactivity of Anatase TiO_2 Nanocrystals by Controlled Hydrogenation-Induced Surface Defects. *ACS Catal.* **2013**, *3*, 2479−2486.
(32) Wei, W.; Yaru, N.; Chunhua, L.; Zhongzi, X. Hydrogenation of TiO_2 Nanosheets with Exposed {001} Facets for Enhanced Photocatalytc Activity. *RSC Adv.* **2012**, *2*, 8286−8288.
(33) Lu, X.; Wang, G.; Zhai, T.; Yu, M.; Gan, J.; Tong, Y.; Li, Y. Hydrogenated TiO_2 Nanotube Arrays for Supercapacitors. *Nano Lett.* **2012**, *12*, 1690−1696.
(34) Yang, S.; Yang, B. X.; Wu, L.; Li, Y. H.; Liu, P.; Zhao, H.; Yu, Y. Y.; Gong, X. Q.; Yang, H. G. Titania Single Crystals with a Curved Surface. *Nat. Commun.* **2014**, *5*, 5355−5361.
(35) Barnard, A.; Zapol, P.; Curtiss, L. Modeling the Morphology and Phase Stability of TiO_2 Nanocrystals in Water. *J. Chem. Theory Comput.* **2005**, *1*, 107−116.
(36) Gong, X.-Q.; Selloni, A. Reactivity of Anatase TiO_2 Nanoparticles: the Role of the Minority (001) Surface. *J. Phys. Chem. B* **2005**, *109*, 19560−19562.
(37) Vittadini, A.; Selloni, A.; Rotzinger, F.; Grätzel, M. Structure and Energetics of Water Adsorbed at TiO_2 Anatase (101) and (001) Surfaces. *Phys. Rev. Lett.* **1998**, *81*, 2954.
(38) Xia, T.; Zhang, C.; Oyler, N. A.; Chen, X. Hydrogenated TiO_2 Nanocrystals: a Novel Microwave Absorbing Material. *Adv. Mater.* **2013**, *25*, 6905−6910.
(39) Xia, T.; Zhang, C.; Oyler, N. A.; Chen, X. Enhancing Microwave Absorption of TiO_2 Nanocrystals via Hydrogenation. *J. Mater. Res.* **2014**, *29*, 2198−2210.
(40) Shen, L.; Uchaker, E.; Zhang, X.; Cao, G. Hydrogenated $Li_4Ti_5O_{12}$ Nanowire Arrays for High Rate Lithium Ion Batteries. *Adv. Mater.* **2012**, *24*, 6502−6506.
(41) Zheng, Z.; Huang, B.; Lu, J.; Wang, Z.; Qin, X.; Zhang, X.; Dai, Y.; Whangbo, M.-H. Hydrogenated Titania: Synergy of Surface Modification and Morphology Improvement for Enhanced Photocatalytic Activity. *Chem. Commun.* **2012**, *48*, 5733−5735.
(42) Zhao, Y.; Zhang, Y.; Liu, H.; Ji, H.; Ma, W.; Chen, C.; Zhu, H.; Zhao, J. Control of Exposed Facet and Morphology of Anatase Crystals through TiO_xF_y Precursor Synthesis and Impact of the Facet on Crystal Phase Transition. *Chem. Mater.* **2014**, *26*, 1014−1018.
(43) Lu, Z.; Yip, C. T.; Wang, L.; Huang, H.; Zhou, L. Hydrogenated TiO2 Nanotube Arrays as High-Rate Anodes for Lithium-Ion Microbatteries. *ChemPlusChem* **2012**, *77*, 991−1000.
(44) Wang, Z.; Wen, B.; Hao, Q.; Liu, L.-M.; Zhou, C.; Mao, X.; Lang, X.; Yin, W.-J.; Dai, D.; Selloni, A. Localized Excitation of Ti^{3+} Ions in the Photoabsorption and Photocatalytic Activity of Reduced Rutile TiO_2. *J. Am. Chem. Soc.* **2015**, *137*, 9146−9152.
(45) Islam, M. M.; Calatayud, M.; Pacchioni, G. Hydrogen Adsorption and Diffusion on the Anatase TiO_2 (101) Surface: a First-Principles Investigation. *J. Phys. Chem. C* **2011**, *115*, 6809−6814.
(46) Aschauer, U.; Selloni, A. Hydrogen Interaction with the Anatase TiO_2 (101) Surface. *Phys. Chem. Chem. Phys.* **2012**, *14*, 16595−16602.
(47) Lu, Y.; Yin, W.-J.; Peng, K.-L.; Wang, K.; Hu, Q.; Selloni, A.; Chen, F.-R.; Liu, L.-M.; Sui, M.-L. Self-Hydrogenated Shell Promoting Photocatalytic H_2 Evolution on Anatase TiO_2. *Nat. Commun.* **2018**, *9*, 2752−2760.
(48) Wang, Z.; Yang, C.; Lin, T.; Yin, H.; Chen, P.; Wan, D.; Xu, F.; Huang, F.; Lin, J.; Xie, X. H-Doped Black Titania with Very High Solar Absorption and Excellent Photocatalysis Enhanced by Localized Surface Plasmon Resonance. *Adv. Funct. Mater.* **2013**, *23*, 5444−5450.
(49) Akimoto, J.; Gotoh, Y.; Oosawa, Y.; Nonose, N.; Kumagai, T.; Aoki, K.; Takei, H. Topotactic Oxidation of Ramsdellite-Type $Li_{0.5}TiO_2$, a New Polymorph of Titanium Dioxide: TiO_2 (R). *J. Solid State Chem.* **1994**, *113*, 27−36.
(50) Peng, C.-W.; Richard-Plouet, M.; Tsai, M.-C.; Lee, C.-Y.; Chiu, H.-T.; Petit, P.-E.; Sheu, H.-S.; Lefrant, S.; Brohan, L. Interconversion of Rutile TiO_2 and Layered Ramsdellite-Like Titanates: New Route to Elongated Mesoporous Rutile Nanoplates. *Cryst. Growth Des.* **2008**, *8*, 3555−3559.
(51) Latroche, M.; Brohan, L.; Marchand, R.; Tournoux, M. New Hollandite Oxides: TiO_2 (H) and $K_{0.06}TiO_2$. *J. Solid State Chem.* **1989**, *81*, 78−82.
(52) Ma, S.; Huang, S.-D.; Fang, Y.-H.; Liu, Z.-P. Microporous Titania Crystals with Penta-oxygen Coordination. *ACS Appl. Energy Mater.* **2018**, *1*, 22−26.

DOI: 10.1021/acscatal.8b03077
ACS Catal. 2018, 8, 9711−9721